AGU PUBLICATIONS

Geophysical Research Letters

RESEARCH LETTER
10.1002/2016GL068388

Key Points:
- Observed CO_2 density and temperature agree well with model predictions
- Sensitivity of temperature and density on physical parameters is explored
- Longitudinal disturbances represent a stationary imprint of topography in the thermosphere

Supporting Information:
- Figure S1

Correspondence to:
A. S. Medvedev,
medvedev@mps.mpg.de

Citation:
Medvedev, A. S., et al. (2016), Comparison of the Martian thermospheric density and temperature from IUVS/MAVEN data and general circulation modeling, *Geophys. Res. Lett.*, *43*, doi:10.1002/2016GL068388.

Received 22 FEB 2016
Accepted 22 MAR 2016
Accepted article online 4 APR 2016

©2016. American Geophysical Union. All Rights Reserved.

Comparison of the Martian thermospheric density and temperature from IUVS/MAVEN data and general circulation modeling

Alexander S. Medvedev[1,2], Hiromu Nakagawa[3], Chris Mockel[1], Erdal Yiğit[1,4], Takeshi Kuroda[1,3], Paul Hartogh[1], Kaori Terada[3], Naoki Terada[3], Kanako Seki[5], Nicholas M. Schneider[6], Sonal K. Jain[6], J. Scott Evans[7], Justin I. Deighan[6], William E. McClintock[6], Daniel Lo[8], and Bruce M. Jakosky[6]

[1]Max Planck Institute for Solar System Research, Göttingen, Germany, [2]Institute of Astrophysics, Georg-August-Universität Göttingen, Göttingen, Germany, [3]Department of Geophysics, Tohoku University, Sendai, Japan, [4]Department of Physics and Astronomy, George Mason University, Fairfax, Virginia, USA, [5]Department of Earth and Planetary Science, University of Tokyo, Tokyo, Japan, [6]Laboratory for Atmospheric and Space Physics, University of Colorado Boulder, Boulder, Colorado, USA, [7]Computational Physics, Inc., Springfield, Virginia, USA, [8]Lunar and Planetary Laboratory, University of Arizona, Tucson, Arizona, USA

Abstract Newly released Imaging Ultraviolet Spectrograph/Mars Atmosphere and Volatile EvolutioN (IUVS/MAVEN) measurements of CO_2 density in the Martian thermosphere have been used for comparison with the predictions of the Max Planck Institute Martian General Circulation Model (MPI-MGCM). The simulations reproduced (within one standard deviation) the available zonal mean density and derived temperature above 130 km. The MGCM replicated the observed dominant zonal wave number 3 nonmigrating tide and demonstrated that it represents a nonmoving imprint of the topography in the thermosphere. The comparison shows a great dependence of the simulated density and temperature to the prescribed solar flux, atomic oxygen abundances and gravity wave effects, with the former two being especially important in the thermosphere above 130 km and the latter playing a significant role both in the mesosphere and thermosphere.

1. Introduction

The Martian thermosphere is the least studied region of Mars' atmosphere. It connects the denser lower atmosphere with the exosphere, where atmospheric species are lost into space. Dynamical processes in the thermosphere control the upward transport of these constituents and, therefore, are important for understanding and quantifying the degree of atmospheric loss. On the practical side, the thermosphere is the region where spacecraft perform aerobraking operations to reduce their speed and form orbits. An accurate knowledge of the state of the thermosphere and of the physical mechanisms influencing its structure is, thus, important for planning such operations, reducing the amount of the required fuel, and for the safety of orbiters and instruments they carry.

Much of the information about the thermospheric density and neutral temperature on Mars and their variability has been collected from aerobraking [e.g., *Keating et al.*, 1998; *Angelats i Coll et al.*, 2004], radio occultation [e.g., *Bougher et al.*, 2004], and stellar occultation [e.g., *Forget et al.*, 2009; *González-Galindo et al.*, 2009; *Gröller et al.*, 2015] measurements on board several recent Martian orbiters. The Mars Atmosphere and Volatile EvolutioN (MAVEN) mission, which has operated for slightly over 1 year to date, has been specifically designed to investigate the upper atmosphere. The Imaging Ultraviolet Spectrograph (IUVS) [*McClintock et al.*, 2014] on board MAVEN measures spectra of mid-UV and far UV atmospheric emissions, which are used for retrieving vertical density profiles of CO_2 and other species. This work reports on the analyses of the first set of data obtained with the instrument and on their comparison with results of simulations with the Max Planck Institute Martian General Circulation Model (MPI-MGCM) that extends from the ground into the thermosphere. This comparison is essential for testing our current understanding of processes occurring in the thermosphere and for constraining them in the MGCM.

The paper is structured as follows. Section 2 describes the IUVS data set utilized in the analyses presented here. The MPI-MGCM is outlined in section 3. The CO_2 density results are given in section 4, while the derived temperatures are compared in section 5. In section 6, we present the findings for the longitudinal variations of density and temperature. Finally, conclusions are presented in section 7.

2. Imaging Ultraviolet Spectrograph (IUVS) Data

IUVS measures the far and mid-UV day airglow within the 110 to 340 nm wavelength range, from which vertical profiles of density for various molecules are retrieved along with the estimates of random uncertainties, as described in the work of *Evans et al.* [2015]. Random uncertainties are defined as errors that follow a Gaussian spread on the time scale of the measurements and, therefore, cannot be assumed to be constant. Contrary, systematic uncertainties have been established during the calibration phase of the instrument and are considered to be constant at 30% of the magnitude of the actual measurement at this stage.

In this paper, we focus on the October 2014 campaign (orbit numbers 109 to 128), in which a total of 73 density profiles were obtained for the period between 18 and 22 October (solar longitudes $L_s = 216.68°$ to 218.94°) [*Schneider et al.*, 2015]. The data set has also been utilized (and described in more detail) in the paper of *Lo et al.* [2015]. The measurements were taken during the periapsis orbit phases, which corresponded to early local afternoon (local times LT between 13.519 and 14.198 h). The locations of the IUVS line-of-sight limb scans span all latitudes between the equator and ~30°N and are distributed almost uniformly across all longitudes. CO_2 number density profiles have been retrieved from the CO_2^+ Ultraviolet Doublet emissions (UVD, 288–289 nm) [*Jain et al.*, 2015], which were constrained to solar zenith angles SZA $< 60°$ [*Evans et al.*, 2015]. These level 2 (version 03) vertical profiles of CO_2 number density are the starting point of our consideration.

3. Max Planck Institute Martian General Circulation Model (MPI-MGCM)

The MPI-MGCM solves the nonlinear primitive equations on the globe using a spectral method. The model was described in detail in the works of *Hartogh et al.* [2005, 2007] and *Medvedev and Hartogh* [2007]. In the vertical direction, its domain is represented by 67 hybrid levels (terrain following in the lower atmosphere and pressure levels in the upper atmosphere), which extend from the surface up to the top pressure level of $p = 3.6 \times 10^{-6}$ Pa. No material flux is assumed across the upper boundary (zero vertical velocities at the top ghost level). Given strong molecular diffusion in the thermosphere, mainly the solution at the top level is affected by the model lid. In the horizontal, a T21 spectral resolution (64 and 32 grid points in longitude and latitude, respectively) has been used in the simulations. The model contains a set of physical parameterization suitable for the atmosphere from the ground up to the thermosphere. The adopted values of the following parameters can be important for interpreting the simulation results: the CO_2-O quenching rate coefficient $k_{VT} = 3.0 \cdot 10^{-12}$ cm^3 s^{-1} used in the non-local thermodynamic equilibrium (non-LTE) radiation heating/cooling scheme and the UV heating efficiency factor of 0.22. It is the only MGCM to date that includes a nonlinear parameterization of the effects of subgrid-scale gravity waves (GWs) with broad spectra [*Yiğit et al.*, 2008]. The parameterization has been specifically developed for "whole atmosphere" models and was extensively tested both in the terrestrial context [*Yiğit et al.*, 2009, 2012, 2014; *Yiğit and Medvedev*, 2009, 2010, 2012] and for Mars [*Medvedev and Yiğit*, 2012; *Medvedev et al.*, 2013, 2015; *Yiğit et al.*, 2015a]. Most recently, the whole atmosphere parameterization has been used to interpret Martian high-altitude GW observations conducted by MAVEN [*Yiğit et al.*, 2015b].

For comparisons with the IUVS data, the model was run for 50 sols before the dates of the corresponding measurements keeping model parameters constant as described in the next section to ensure an appropriate spinup. In all the simulations, we utilized the observed seasonally and latitudinally varying dust optical depth averaged over Martian Years from MY = 24 and 31 (excluding major dust storms), which was converted to the vertically varying dust volume mixing ratio according to the Conrath formula [*Conrath*, 1975]. The other details of the numerical experiments and the status of physical parameterizations were the same as in the most recent applications of the MGCM [*Medvedev et al.*, 2015; *Yiğit et al.*, 2015a]. The model output emulated the IUVS observations, that is, was taken at the same solar longitudes, local times, and locations.

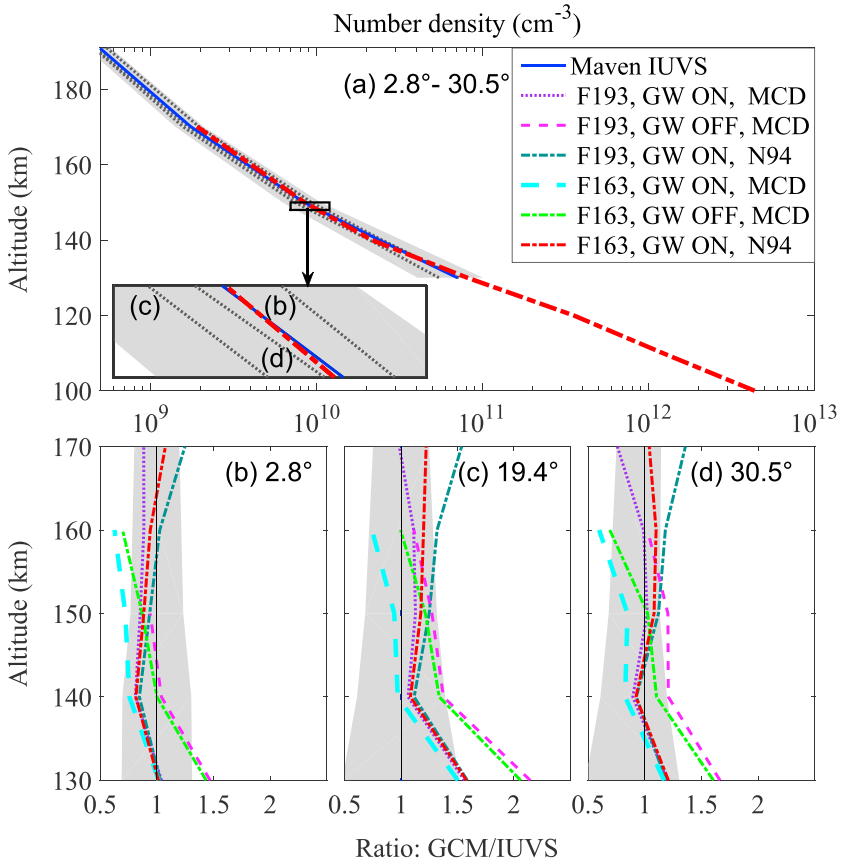

Figure 1. Zonal mean CO_2 number density (a) averaged between 2.8° and 30°N; (b–d) the individual bins centered at the indicated latitudes. Blue solid lines and gray shadings are for the IUVS mean density and 1 standard deviations $\pm\sigma$, respectively. In Figure 1a, black dotted lines show the observed zonal means for the latitudinal bins given in the bottom panels. Figures 1b–1d display the ratio between the modeled and observed number density for the simulations listed in the caption.

4. CO_2 Density

The vertical profiles of CO_2 number density retrieved from the IUVS data are given between 80 and 600 km with the 10 km resolution below 150 km and an increasing step above this mark. Above ~220 km and below ~130 km, the level of noise (random uncertainties) steeply increases due to declining airglow signal. Therefore, the region with the lowest random uncertainties (between 130 and 200 km) was chosen for the main analysis.

At first, we analyze zonally averaged (i.e., over all longitudes at a given latitude) densities. The already small error due to random uncertainties is further mitigated through averaging by a factor of $\sqrt{N}$, where N is the number of measurements in the ensemble. The remaining errors can then be attributed to the systematic uncertainties. Note that the calibration (systematic) uncertainty is applicable to all points in a group of observations. In other words, it characterizes systematic biases of retrieved density, the values of which might be larger or smaller by the magnitude of uncertainty at all heights simultaneously. The results for zonally averaged CO_2 densities are plotted in Figure 1. The blue line in Figure 1a represents the IUVS density averaged over all longitudes and between all available latitudes (0–30°N); the gray shading displays 1 standard deviation σ of the measurements with respect to the mean. For comparison, the mean profiles for three latitudinal bins centered at 2.8°N (12 profiles), 19.4°N (18 profiles), and 30.5°N (10 profiles) are also plotted with black dotted lines.

Before comparing with model simulations, we discuss the major physical mechanisms that affect the upper atmosphere and, thus, must be represented and constrained in the MGCM. First, the solar radiation flux influences the absorption by molecules in the thermosphere and, therefore, temperature and density. Solar activity enters the model in the form of the $F_{10.7}$ solar radio emission index, the particular values of which for the

Table 1. Daily Mean $F_{10.7}$ Solar Flux Index at the Dates of Observations[a]

Date	$F_{10.7}$ Index	Date	$F_{10.7}$ Index
2014/10/17	145.8	2014/10/20	204.0
2014/10/18	172.4	2014/10/21	199.0
2014/10/19	173.1	2014/10/22	216.3

[a]Dates are formatted as year/month/day.

period of observations are given in Table 1. The available IUVS measurements in October 2014 coincided with the occurrence of an M-class solar flare. Hence, the solar activity rose rapidly and varied strongly during the observational campaign. It is obviously difficult to synchronize the timing of observations and model output, and our goal was not to capture transient events. Therefore, we chose two representative $F_{10.7}$: one corresponds to the beginning of measurements (10 sol average, $F_{10.7} = 163 \times 10^{-22}$ W m^2 Hz^{-1} at Earth) and one to the average over the period of observations ($F_{10.7} = 193 \times 10^{-22}$ W m^2 Hz^{-1} at Earth). These values were kept constant during the entire period of simulations, including 50 sols of spin-up.

The second factor that strongly affects thermospheric temperature and density is the amount of atomic oxygen. It influences the non-LTE radiative transfer in IR bands of CO_2 molecules, which is the main radiative mechanism of heating and cooling in the thermosphere. Because IUVS retrievals of atomic oxygen were not available at the time of our analyses, we used two representative vertical profiles, which were discussed in detail in the paper of *Medvedev et al.* [2015, Figure 1]. One profile is based on the one-dimensional photochemical model of *Nair et al.* [1994] and has extensively been utilized by many MGCMs [e.g., *Angelats i Coll et al.*, 2005; *Bell et al.*, 2007; *González-Galindo et al.*, 2010; *McDunn et al.*, 2010]. The other was derived from Mars Climate Database (MCD) [*González-Galindo et al.*, 2009], represents larger concentrations of oxygen, and results in stronger cooling by CO_2. Recent globally averaged measurements [*Rezac et al.*, 2015; *Mahaffy et al.*, 2015] hint that oxygen density profiles lie somewhere between the Nair and MCD models. We denote these scenarios in our discussions as N94 and MCD, correspondingly.

The third mechanism in the thermosphere that must be taken into account concerns the effects of small-scale gravity waves (GWs). These waves originate from a variety of sources in the lower atmosphere such as flow over topography, instabilities of weather systems, nonlinear wave-wave interactions, and convection. Upon vertical propagation, they grow in amplitude, break, and/or dissipate. The momentum and energy they carry are then deposited into the mean flow, and the sensible heat flux they induce causes a redistribution of heat in the thermosphere. The effects of GWs on neutral temperature (and density) are complex; they include modifications of temperature associated with changes in circulation patterns [*Medvedev et al.*, 2011], heating due to dissipation of their kinetic energy, and heating/cooling due to the induced heat fluxes [*Medvedev and Yiğit*, 2012]. Overall, the thermal effects of GWs in Mars' atmosphere lead to an enhancement of middle atmosphere polar warmings, strong cooling in polar regions of the thermosphere [*Medvedev et al.*, 2015], and sometimes weak warmings in low latitudes of the upper atmosphere [*Medvedev et al.*, 2013]. Hence, GW physics is interactively included in our selected simulations, which are designated as GW ON. The nomenclature of six representative simulations used for this comparison with the IUVS measurements is shown in the legend in Figure 1.

Above 130 km, all the simulations produced densities in a reasonably good agreement with the observations (that is, within 1 standard deviation from the mean). In Figure 1a, one of the profiles that qualitatively better reproduce the observations ("F163, GW ON, N94") is shown in red. Figures 1b–1d present a more detailed comparison for all runs in the form of ratios of the simulated and observed values for the three latitudinal bins. Despite the differences between the runs, the simulated density profiles fit the observations above 130 km within a few tens of percent and, in many cases, within the data standard deviations. The increasing mismatch below 140 km is due to the deterioration of accuracy of retrievals below the peak emission. The agreement between the modeling and observations is better for the near-equatorial bin but worsens with increasing latitude.

Now we turn to a more detailed inspection of the MGCM runs. The first thing that stands out is that some profiles extend higher than others. This reflects a vertical expansion of the atmosphere at higher temperatures, when individual model pressure levels move farther upward. An extension to ~170 km occurs in three runs that generated the warmest thermosphere: all of them include GWs, two are for higher solar activity (F193), and two employ the low atomic oxygen scenario N94. In the other three experiments, the model top does not

extend above ~160 km, in average, due to the colder simulated thermosphere. Comparing the counterpart simulations for the lower and higher solar activity, one can easily see that larger solar fluxes result in larger densities, and these effects increase with height.

The sensitivity of the simulated density to atomic oxygen variations is very similar to the response to solar activity. Smaller atomic oxygen abundances (N94 scenario) lead to a weaker cooling by CO_2, higher temperature, and larger densities. This effect also depends on altitude and is appreciable above ~140 km.

The influence of GWs on density is the most significant compared to the above two mechanisms at all heights. Inclusion of GW effects decreases the simulated densities in concordance with the results from the recent study of *Medvedev et al.* [2015] and helps to bring the simulations closer to the observations. Note that a similar result was obtained for lower altitudes (around 120 km), where accounting for thermal effects of GWs helped to reproduce temperatures obtained from Mars Odyssey aerobraking measurements [*Medvedev and Yiğit*, 2012], which had not been possible with the previous modeling efforts that had not included these effects.

Overall, the presented analyses regarding the processes in the upper atmosphere reveal two important results. First, the observed densities (including their variances) are within the range of variability due to uncertainties of model parameters. This finding indicates that the MGCM captures the thermospheric physics well, at least at the altitudes where observations and simulations overlap. Second, GW effects are very important, but least constrained in the model. For instance, GW sources were assumed to be uniformly distributed in the lower atmosphere, whereas recent high-resolution (GW-resolving) simulations of *Kuroda et al.* [2015] indicate that the sources can greatly vary with latitude and season. We proceed to the comparison with the derived IUVS temperature in the next section.

5. Neutral Temperature

Temperature profiles $T(z)$ have been derived from density $\rho(z)$ by integrating the hydrostatic equation, $dp/dz = -\rho g$, and using the ideal gas law $p = \rho RT$, where p is pressure, $R = 191.2$ J kg^{-1} K^{-1} is the specific gas constant for a pure CO_2 atmosphere, and $g(z)$ is the vertically varying acceleration of gravity. The integration has been performed for each profile $\rho(z)$ from the top downward using the Runge-Kutta-Fehlberg integrator (RKF45). This procedure requires an analytic expression for the density, which was obtained by interpolating between the measurement points. The integration requires prescribing temperature at the top, the value of which is unknown. However, solutions at lower altitudes are insensitive to the choice of the initial condition at the upper boundary, as was also discussed in the paper of *Forget et al.* [2009]. Figure 2a illustrates this for an individual profile: the solutions for temperature converge within a few scale heights regardless of the value at the top and are practically indistinguishable below ~190 km. We used $T = 260$ K at 220 km in all our calculations.

The temperature analysis was performed in a manner similar to density (same zonal bands, same simulation conditions), and the results are presented in Figure 2. It illustrates the sensitivity of the simulations to variations of model parameters. Several combinations of them produce temperature profiles that match the observations within 1 standard deviation in the average sense (Figure 2b) and for the individual latitude bins (Figures 2c–2e). Among them, two combinations ("F163, N94" and "F193, MCD") yield a better fit, as was also the case with the CO_2 density analysis. This, however, does not exclude that other possible combinations and finer tuning can result in even better agreement, which is not the goal of this paper.

Now we consider closer the influence of thermospheric physics on the simulated temperature. The response of temperature to variations of solar activity is straightforward and in line with expectations: larger solar fluxes produce larger temperature, and this positive feedback grows with height in the region where atomic oxygen is transitioning from a trace gas to a main constituent in the upper atmosphere (above 140 km). The warming effect of the "low atomic oxygen" N94 scenario has already been discussed in the previous section. It is seen that the magnitudes of temperature changes associated with varying oxygen are of the same order as those induced by the altered solar flux. For practical purposes of MGCM modeling, both mechanisms should be carefully constrained. Unlike with the $F_{10.7}$ index, which is constantly monitored, atomic oxygen concentration and its variations are poorly known in the Martian thermosphere. Our results illustrate the importance of having simultaneous measurements of temperature and atomic oxygen abundances.

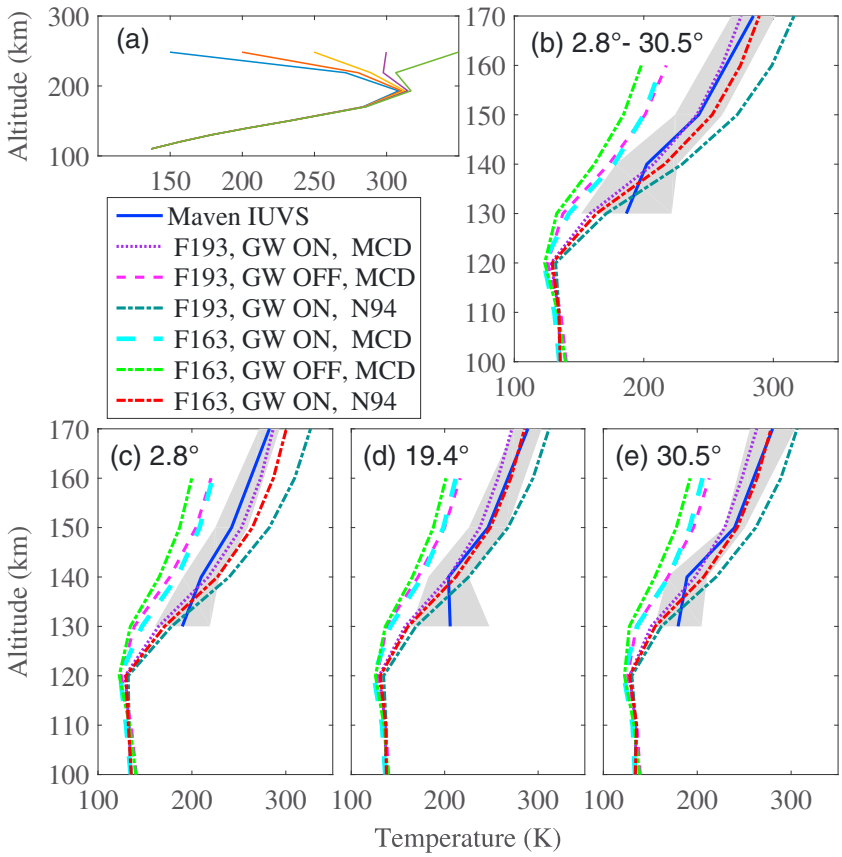

Figure 2. Comparison of temperature profiles: (a) illustration of the convergence of the solution for temperature (below ~190), in kilometer, for a single observed density profile regardless of the initial conditions at the top; (b) comparison of zonal mean temperatures averaged between 2.8° and 30°N from the IUVS observations (blue) and simulated with the MGCM. (c–e) The same as in Figure 2b but for the indicated zonal bins. Gray shadings show 1 standard deviation for the IUVS measurements ($\pm\sigma$).

The simulations demonstrate a great and complex dependence of temperature on parameterized GWs. Contrary to the notion that the main effect of these waves is cooling, a comparison of the counterpart simulations, i.e., with GW ON and GW OFF, shows that the inclusion of GW physics results in a temperature increase. Further inspection of Figures 2c–2e reveals that this effect also depends on latitude: heating is stronger near the equator, but decreases toward higher latitudes. A similar effect of GWs has been modeled in the terrestrial thermosphere [*Yiğit and Medvedev*, 2009]. Figure S1a of the supporting information presents the latitude-altitude cross section of the zonally averaged temperature along with the temperature difference between the simulations with and without GWs. It illustrates that GWs induce strong cooling at midlatitudes and, especially, high latitudes, whereas they result in heating in the equatorial region. This warming in low latitudes is weaker for lower solar activity [*Medvedev et al.*, 2013, Figure 1h], and increases with the latter. Figure S1b in the supporting information demonstrates that the GW-induced temperature enhancement occurs on the dayside and is strongest around local times when the IUVS measurements were taken. On the nightside, GWs induce local cooling in midlatitudes. Such complexity of GW effects is the result of atmospheric dynamics in the underlying layers, through which harmonics originating in the lower atmosphere propagate [*Yiğit and Medvedev*, 2015].

6. Longitudinal Variability

The IUVS observations cover all the longitudes almost uniformly, at almost constant local times (between 13.519 and 14.198 h). Therefore, the data set is very suitable for analyzing the longitudinal variability of density and temperature associated with nonmigrating tides. Previous GCM simulations demonstrated that nonmigrating tides can have a substantial impact on the Martian lower thermosphere

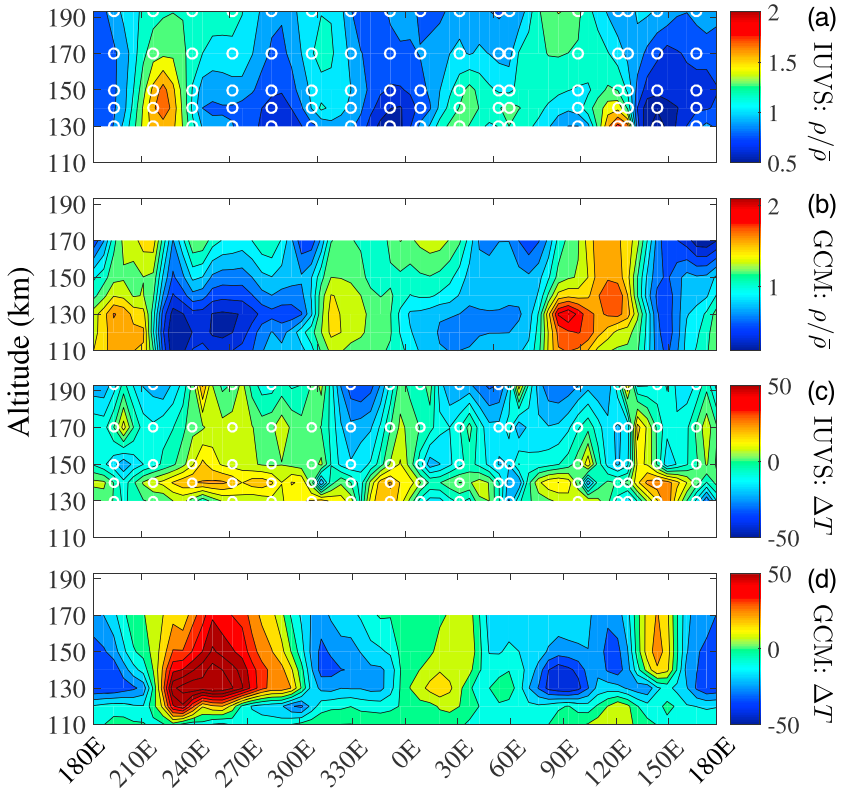

Figure 3. Longitude-altitude cross sections of the observed and simulated density and temperature at 19.4°N. (a) The IUVS density variations $\rho/\bar{\rho}$, where $\bar{\rho}$ is the zonal mean; (b) Same as Figure 3a but for the MGCM simulations; (c) temperature disturbances $\Delta T = T - \bar{T}$ derived from the IUVS measurements; (d) same as in Figure 3c but for the MGCM output. Circles in the Figures 3a and 3c indicate the location of IUVS measurements.

[*Moudden and Forbes*, 2008]. Tidal disturbances can be represented on a globe with the Fourier series as a sum of harmonics $A_{ns}\cos(n\Omega t+s\lambda+\varphi_{ns})$, where λ is the longitude, A_{ns} and φ_{ns} are the amplitude and phase, respectively, of harmonics with zonal wave numbers $s = 0, \pm1, \pm2, \ldots$ and frequencies $n\Omega \equiv 2\pi n/24$ h, $n = 1, 2, 3, \ldots$ In the reference frame of local time $t_{LT} = t + \lambda/\Omega$, this yields a sum of the following harmonics

$$A_{ns}\cos\left[n\Omega t_{LT} + (s-n)\lambda + \varphi_{ns}\right]. \quad (1)$$

For migrating Sun-synchronous tides, $s = n$. Therefore, any longitudinal dependence at a given t_{LT} can be attributed to nonmigrating tides with $s \neq n$.

Density and temperature deviations from the zonal mean are shown at 19.4°N in Figures 3a and 3c, correspondingly. This zonal band was favored due to the good longitudinal coverage with 18 individual profiles that are present at this latitude. They are compared with density and temperature deviations produced by the simulation (F163, GW ON, N94) in Figures 3b and 3d, respectively. The circles mark the locations where the actual IUVS measurements were taken. They illustrate that the observed longitudinal dependencies are sufficiently spatially resolved. The density profiles are plotted in the form of $\rho/\bar{\rho} = (\rho' + \bar{\rho})/\bar{\rho}$, with bars and primes denoting zonally averaged quantities and deviations, respectively. Temperature disturbances are presented directly in the form of T'.

A visual examination of Figure 3a shows a dominant mode with the zonal wave number 3. Fourier analysis reveals that wave number 2 is the next strongest mode in the density variations. The simulated density in Figure 3b reproduces to a certain order the observed features. It is also dominated by the disturbances with the zonal wave number 3, whose magnitude and phase (locations of peaks and troughs) are sufficiently close to those from the observations. The observed temperature variations in Figure 3c are somewhat noisier, but they also demonstrate a clear nonmigrating tide signal and a reasonable degree of similarity with the

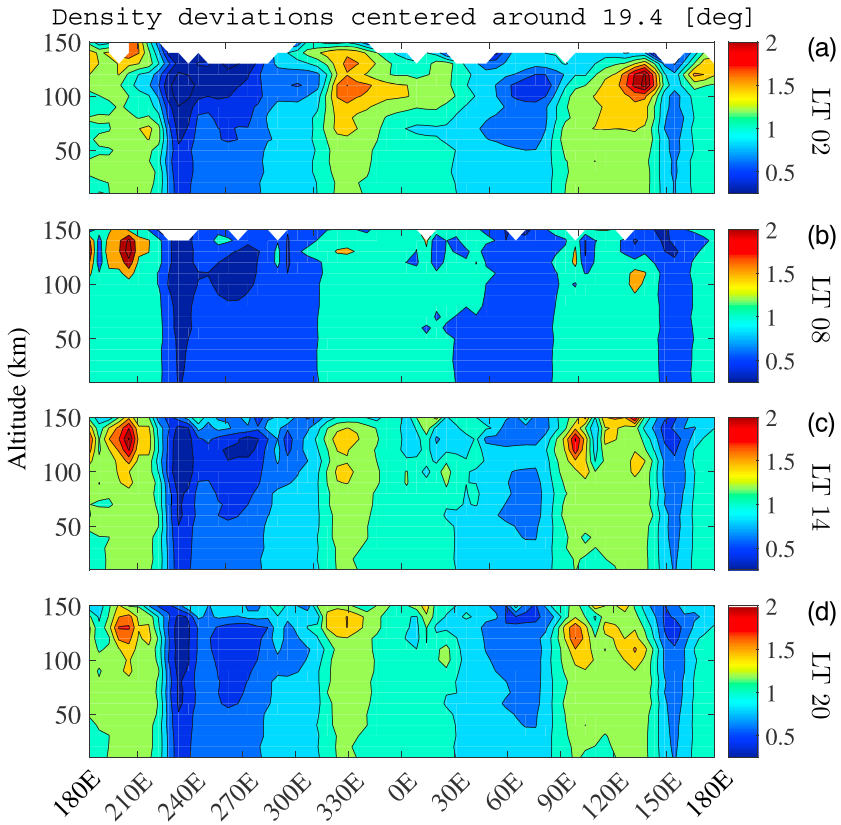

Figure 4. Simulated longitude-altitude cross sections of the nonzonal CO_2 density deviations $\rho/\bar{\rho}$ (as in Figure 3) at 19.4°N at four local times (LT = 02, 08, 14, and 20 h) and in the entire model domain.

simulations, e.g., between 210°E and 0°, and between 30°E and 150°E. Note the anticorrelation between anomalies of density and temperature at these longitudes: regions with lower densities have higher temperatures and vice versa.

Nonmigrating tidal signatures in the IUVS October 2014 data (only the earlier Version 2) have also been reported by *Lo et al.* [2015]. What is the source of these longitudinal disturbances? Obviously, no information about frequencies $n\Omega$ can be derived directly from the observations because they were obtained at approximately same local time t_{LT}. With that, the dominant wave number $(s - n) = 3$ as well as other modes cannot be unambiguously attributed to particular nonmigrating tidal harmonics (s, n). *Lo et al.* [2015] have used information on latitudinal variations of radiation intensities to find structures reminiscent of nonmigrating components of DE2, SE1 and S0 tides. In this study, no robust latitudinal analysis could be performed due to the limited longitudinal coverage outside of the 13° and 19.4°N band. Instead, we used the MGCM, in which the disturbances can be looked at in the entire domain from the surface to the upper boundary in simulations. We performed such analyses and found that the wave number 3 feature shown in Figures 3b and 3c does not move with local time. This implies that $n = 0$ and $s = 3$ for the dominant nonmigrating harmonic. Simulations also reveal that the disturbances can be traced down to the surface and that they are clearly linked to the topography, which is also dominated by wave number 3 features at these latitudes. This is demonstrated in Figure 4 where the simulated density variations are shown at four local times (LT = 02, 08, 14, and 20 h) and in the entire model domain. In particular, the density minimum between 210°E and 300°E is related to the mountainous region, while the maximum between 60°E and 90°E originates over the Syrtis Major. Hence, the model simulations indicate that the longitudinal disturbances revealed by the IUVS observations represent a stationary tropospheric imprint in the upper atmosphere. Are they a result of a direct propagation of the stationary planetary wave from the surface [*Keating et al.*, 1998] or generated in the thermosphere by nonlinear interactions of the diurnal propagating tide and the eastward propagating Kelvin wave with the wave number 2, as was suggested in the work by *Forbes and Hagan* [2000] and supported by observations [*Withers et al.*, 2003] and the GCM modeling of *Angelats i Coll et al.* [2004]? It should be noted that the Kelvin wave is itself generated

nonlinearly in the lower atmosphere by the diurnal tide and topography. Upon propagation, it increases in amplitude, as does the diurnal tide, and the direction of energy exchange within the triad can reverse to maintain the steady component at higher altitudes. This mechanism can act together with the direct propagation of the steady topographically induced disturbances to produce the result seen in Figure 4. A separate in-depth study is required to explain the origin of the nonzonal disturbances measured by the IUVS instrument.

7. Conclusions

We presented the results of an analysis of the first set of data obtained for the Martian thermosphere with the Imaging Ultraviolet Spectrograph (IUVS) instrument on board Mars Atmosphere Volatile EvolutioN (MAVEN) spacecraft over the October 2014 campaign. This data set is closely compared with the simulations using the Max Planck Institute Martian General Circulation Model (MPI-MGCM). With the inferences from the presented model simulations and the IUVS/MAVEN observations, the following conclusions can be drawn:

1. The observed zonal mean CO_2 density and the derived temperature agree well (within 1 standard deviation) with those simulated by the model above ~130 km.
2. The comparison demonstrated a sensitivity of simulated density and temperature profiles on solar flux, atomic oxygen abundances, and gravity wave effects. The former two are especially important above 130 km, whereas the latter are crucial below as well.
3. Longitudinal disturbances with a dominant zonal wave number- 3 mode in density and temperature time associated with nonmigrating tides are reproduced by the model. The identification of the tide is impossible to perform based on observations at the only fixed local time. However, the MGCM simulations show that this structure does not move with time, extends from the lower atmosphere, and has a similar spectrum as the underlying topography. Thus, at least in the simulations, it represents a stationary imprint of the Martian topography in the thermosphere.

This comparison confirms that the MPI-MGCM can reproduce the state and variability of the Martian thermosphere based on the current state of knowledge of Martian thermosphere physics. The first set of IUVS measurements covers only a limited latitudinal region at a certain season and local time. Further observations will help to constrain physical parameterizations and improve modeling capabilities.

Acknowledgments
IUVS/MAVEN data are archived in the Planetary Atmospheres Node of the Planetary Data System (http://pds-atmospheres.nmsu.edu). Modeling data supporting the figures are available upon request from A.S.M. (medvedev@mps.mpg.de). The work was partially supported by German Science Foundation (DFG) grant ME2752/3-1. E.Y. was partially supported by NASA grant NNX13AO36G.

References

Angelats i Coll, M., F. Forget, M. A. López-Valverde, P. L. Read, and S. R. Lewis (2004), Upper atmosphere of Mars up to 120 km: Mars Global Surveyor accelerometer data analysis with the LMD general circulation model, *J. Geophys. Res.*, *109*, E01011, doi:10.1029/2003JE002163.

Angelats i Coll, M., F. Forget, M. A. López-Valverde, and F. González-Galindo (2005), The first Mars thermospheric general circulation model: The Martian atmosphere from the ground to 240 km, *Geophys. Res. Lett.*, *32*, L04201, doi:10.1029/2004GL021368.

Bell, J. M., S. W. Bougher, and J. R Murphy (2007), Vertical dust mixing and the interannual variations in the Mars thermosphere, *J. Geophys. Res.*, *112*, E12002, doi:10.1029/2006JE002856.

Bougher, S. W., S. Engel, D. P. Hinson, and J. R. Murphy (2004), MGS Radio Science electron density profiles: Interannual variability and implications for the Martian neutral atmosphere, *J. Geophys. Res.*, *109*, E03010, doi:10.1029/2003JE002154.

Conrath, B. J. (1975), Thermal structure of the Martian atmosphere during the dissipation of the dust storm of 1971, *Icarus*, *24*, 36–46.

Evans, J. S., et al. (2015), Retrieval of CO_2 and N_2 in the Martian thermosphere using dayglow observations by IUVS on MAVEN, *Geophys. Res. Lett.*, *42*, 9040–9049, doi:10.1002/2015GL065489.

Forbes, G. M., and M. E. Hagan (2000), Diurnal Kelvin wave in the atmosphere of Mars: Towards an understanding of the stationary density structures observed by the MGS accelerometer, *Geophys. Res. Lett.*, *27*, 3563–3566.

Forget, F., F. Montmessin, J.-L. Bertaux, F. González-Galindo, S. Lebonnois, E. Quémerais, A. Reberac, E. Dimarellis, and M. A. López-Valverde (2009), Density and temperatures of the upper Martian atmosphere measured by stellar occultations with Mars Express SPICAM, *J. Geophys. Res.*, *114*, E01004, doi:10.1029/2008JE003086.

González-Galindo, F., F. Forget, M. A. López-Valverde, M. Angelats i Coll, and E. Millour (2009), A ground-to-exosphere Martian general circulation model: 1. Seasonal, diurnal, and solar cycle variation of thermospheric temperatures, *J. Geophys. Res.*, *114*, E04001, doi:10.1029/2008JE003246.

González-Galindo, F., S. W. Bougher, M. A. López-Valverde, F. Forget, and J. Murphy (2010), Thermal and wind structure of the Martian thermosphere as given by two general circulation models, *Planet. Space Sci.*, *58*, 1832–1840.

Gröller, H., et al. (2015), Probing the Martian atmosphere with MAVEN/IUVS stellar occultations, *Geophys. Res. Lett.*, *42*, 9064–9070, doi:10.1002/2015GL065294.

Hartogh, P., A. S. Medvedev, T. Kuroda, R. Saito, G. Villanueva, A. G. Feofilov, A. A. Kutepov, and U. Berger (2005), Description and climatology of a new general circulation model of the Martian atmosphere, *J. Geophys. Res.*, *110*, E11008, doi:10.1029/2005JE002498.

Hartogh, P., A. S. Medvedev, and C. Jarchow (2007), Middle atmosphere polar warmings on Mars: Simulations and study on the validation with sub-millimeter observations, *Planet. Space Sci.*, *55*, 1103–1112.

Jain, S. K., et al. (2015), The structure and variability of Mars upper atmosphere as seen in MAVEN/IUVS dayglow observations, *Geophys. Res. Lett.*, *42*, 9023–9030, doi:10.1002/2015GL065419.

Keating, G. M., et al. (1998), The structure of the upper atmosphere of Mars: In situ accelerometer measurements from Mars Global Surveyor, *Science*, *279*, 1672–1676.

Kuroda, T., A. S. Medvedev, E. Yiğit, and P. Hartogh (2015), A global view of gravity waves in the Martian atmosphere inferred from a high-resolution general circulation model, *Geophys. Res. Lett.*, *42*, 9213–9222, doi:10.1002/2015GL066332.

Lo, D. Y., et al. (2015), Nonmigrating tides in the Martian atmosphere as observed by MAVEN IUVS, *Geophys. Res. Lett.*, *42*, 9057–9063, doi:10.1002/2015GL066268.

Mahaffy, P. R., M. Benna, M. Elrod, R. V. Yelle, S. W. Bougher, S. W. Stone, and B. M. Jakosky (2015), Structure and composition of the neutral upper atmosphere of Mars from the MAVEN NGIMS investigation, *Geophys. Res. Lett.*, *42*, 8951–8957, doi:10.1002/2015GL065329.

McClintock, W. E., N. M. Schneider, G. M. Holsclaw, J. T. Clarke, A. C. Hoskins, I. Stewart, F. Montmessin, R. V. Yelle, and J. Deighan (2014), The Imaging Ultraviolet Spectrograph (IUVS) for the MAVEN mission, *Space Sci. Rev.*, *195*, 75–124, doi:10.1007/s11214-014-0098-7.

McDunn, T. L., S. W. Bougher, J. Murphy, M. D. Smith, F. Forget, J.-L. Bertaux, and F. Montmessin (2010), Simulating the density and thermal structure of the middle atmosphere (<80–130 km) of Mars using the MGCM-MTGCM: A comparison with MEX/SPICAM observations, *Icarus*, *206*, 5–17.

Medvedev, A. S., and P. Hartogh (2007), Winter polar warmings and the meridional transport on Mars simulated with a general circulation model, *Icarus*, *186*, 97–110.

Medvedev, A. S., and E. Yiğit (2012), Thermal effects of internal gravity waves in the Martian thermosphere, *Geophys. Res. Lett.*, *39*, L05201, doi:10.1029/2012GL050852.

Medvedev, A. S., F. González-Galindo, E. Yiğit, A. G. Feofilov, F. Forget, and P. Hartogh (2015), Cooling of the Martian thermosphere by CO_2 radiation and gravity waves: An intercomparison study with two general circulation models, *J. Geophys. Res. Planets*, *120*, 913–927, doi:10.1002/2015JE004802.

Medvedev, A. S., E. Yiğit, T. Kuroda, and P. Hartogh (2013), General circulation modeling of the Martian upper atmosphere during global dust storm, *J. Geophys. Res.*, *118*, 2234–2246, doi:10.1002/2013JE004429.

Medvedev, A. S., E. Yiğit, P. Hartogh, and E. Becker (2011), Influence of gravity waves on the Martian atmosphere: General circulation modeling, *J. Geophys. Res.*, *116*, E10004, doi:10.1029/2011JE003848.

Moudden, Y., and J. M. Forbes (2008), Effects of vertically propagating thermal tides on the mean structure and dynamics of Mars' lower thermosphere, *Geophys. Res. Lett.*, *35*, L23805, doi:10.1029/2008GL036086.

Nair, H., M. Allen, A. D. Anbar, Y. L. Yung, and R. T. Clancy (1994), A photochemical model of the Martian atmosphere, *Icarus*, *111*, 124–150.

Rezac, L., P. Hartogh, R. Güsten, H. Wiesemeyer, H.-W. Hübers, C. Jarchow, H. Richter, B. Klein, and N. Honingh (2015), First detection of the 63 μm atomic oxygen line in the thermosphere of Mars with GREAT/SOFIA, *Astron. Astrophys.*, *580*, L10, doi:10.1051/0004-6361/201526377.

Schneider, N. M., et al. (2015), MAVEN IUVS observations of the aftermath of the Comet Siding Spring meteor shower on Mars, *Geophys. Res. Lett.*, *42*, 4765–4761, doi:10.1002/2015GL063863.

Withers, P., S. W. Bougher, and G. M. Keating (2003), The effects of topographically-controlled thermal tides in the Martian upper atmosphere as seen by the MGS accelerometer, *Icarus*, *164*, 14–32, doi:10.1016/S0019-1035(03)00135-0.

Yiğit, E., and A. S. Medvedev (2009), Heating and cooling of the thermosphere by internal gravity waves, *Geophys. Res. Lett.*, *36*, L14807, doi:10.1029/2009GL038507.

Yiğit, E., and A. S. Medvedev (2010), Internal gravity waves in the thermosphere during low and high solar activity: Simulation study, *J. Geophys. Res.*, *115*, A00G02, doi:10.1029/2009JA015106.

Yiğit, E., and A. S. Medvedev (2012), Gravity waves in the thermosphere during a sudden stratospheric warming, *Geophys. Res. Lett.*, *39*, L21101, doi:10.1029/2012GL053812.

Yiğit, E., and A. S. Medvedev (2015), Internal wave coupling processes in Earth's atmosphere, *Adv. Space Res.*, *55*, 983–1003, doi:10.1016/j.asr.2014.11.020.

Yiğit, E., A. D. Aylward, and A. S. Medvedev (2008), Parameterization of the effects of vertically propagating gravity waves for thermosphere general circulation models: Sensitivity study, *J. Geophys. Res.*, *113*, D19106, doi:10.1029/2008JD010135.

Yiğit, E., A. S. Medvedev, A. D. Aylward, P. Hartogh, and M. J. Harris (2009), Modeling the effects of gravity wave momentum deposition on the general circulation above the turbopause, *J. Geophys. Res.*, *114*, D07101, doi:10.1029/2008JD011132.

Yiğit, E., A. S. Medvedev, A. D. Aylward, A. J. Ridley, M. J. Harris, M. B. Moldwin, and P. Hartogh (2012), Dynamical effects of internal gravity waves in the equinoctial thermosphere, *J. Atmos. Sol. Terr. Phys.*, *90-91*, 104–116, doi:10.1016/j.jastp.2011.11.014.

Yiğit, E., A. S. Medvedev, S. L. England, and T. J. Immel (2014), Simulated variability of the high-latitude thermosphere induced by small-scale gravity waves during a sudden stratospheric warming, *J. Geophys. Res. Space Physics*, *119*, 357–365, doi:10.1002/2013JA019283.

Yiğit, E., A. S. Medvedev, and P. Hartogh (2015a), Gravity waves and high-altitude CO_2 ice cloud formation in the Martian atmosphere, *Geophys. Res. Lett.*, *42*, 4294–4300, doi:10.1002/2015GL064275.

Yiğit, E., S. L. England, G. Liu, A. S. Medvedev, P. R. Mahaffy, T. Kuroda, and B. M. Jakosky (2015b), High-altitude gravity waves in the Martian thermosphere observed by MAVEN/NGIMS and modeled by a gravity wave scheme, *Geophys. Res. Lett.*, *42*, 8993–9000, doi:10.1002/2015GL065307.